Journal of Experimental Nanoscience
Publication details, including instructions for authors and subscription information:
http://www.informaworld.com/smpp/title~content=t716100757

Optimization of diffractive MEMS for optical switching

J. P. Verheggen[a]; W. Khan-Raja[a]; J. Castracane[a]
[a] College of Nanoscale Science and Engineering, Albany, New York

Online publication date: 01 December 2010

Journal of Experimental Nanoscience,
Vol. 2, Nos. 1–2, March–June 2007, 87–100

Taylor & Francis
Taylor & Francis Group

Optimization of diffractive MEMS for optical switching

J. P. VERHEGGEN, W. KHAN-RAJA and J. CASTRACANE*

College of Nanoscale Science and Engineering, University at Albany-SUNY, Albany, New York

(*Received June 2006; in final form September 2006*)

Diffractive Micro-Electro-Mechanical Systems (D-MEMS) have enjoyed increased attention in the fields of communication, spectroscopy, projection display, and maskless lithography. Redirecting an optical signal into predefined angles, precisely balancing this optical signal, inherent wavelength filtering capability and high switching speed are some of the advantages over other optical MEMS. D-MEMS based on customized IC fabrication processes are being used to assemble system-level architectures for integration into mainstream circuitry. The goal of this work is to improve the optical performance while minimizing the power consumption and operational voltage. Operational characteristics of new D-MEMS have achieved a reduction of the optical switching voltage to 2V at a 6.5V bias. Structural modifications through variation in ruling/top-electrode width and spacing have been studied. An alternative structural material, polyimide, is being optimized for further decreasing the operating voltage of the D-MEMS devices.

Keywords: Diffraction gratings; Diffractive MEMS; Optical interconnect; Polyimide; Spectroscopy

1. Introduction

Diffractive MEMS (D-MEMS) is a subset of optical MEMS based on electromechanically reconfiguring the distribution of diffracted optical intensities. The advantage of D-MEMS over other optical MEMS techniques is that it can allow for low power consumption, high switch speed (the speed with which the device goes from the passive state to the active state) and Q-factor because of the inherent low physical ruling deflection required for switching and high electrostatic force per unit area [1]. In addition, the optical response is wavelength sensitive, allowing for spectral filtering capabilities. D-MEMS have been commercialized in the fields of projection displays [2], spectroscopy [3] and direct printing-board writing [4]. The D-MEMS devices fabricated

*Corresponding author. Email: JCastracane@uamail.albany.edu
College of Nanoscale Science and Engineering, University at Albany-SUNY, 255 Fuller Road, Albany, NY-12203

Journal of Experimental Nanoscience
ISSN 1745–8080 print/ISSN 1745–8099 online © 2007 Taylor & Francis
http://www.tandf.co.uk/journals
DOI: 10.1080/17458080601024188

for these applications are based on creating a diffractive surface from a purely reflective surface.

Wavelength sensitive devices like D-MEMS are the key element of current and future optical communication networks that utilize wavelength dependent, electromechanical manipulation and control of light. Future applications of D-MEMS lie in large bandwidth Dense Wavelength Division Multiplexing (DWDM) in optical networks. Free Space Optical Interconnects (FSOI) at the microchip module level have been studied as a possible solution to the electrical interconnect bottleneck that arises from ultra-high-scale integrated circuitry. In addition, MEMS-based active spectroscopy has been investigated for lightweight, low power, active diffractive elements that are capable of achieving high spectral resolution for planetary spectroscopy. The advantage relative to other optical devices is its ability to multiplex and de-multiplex both in the actuation and non-actuation state [2–5].

The first section of the paper focuses on polysilicon-based diffractive MEMS beginning with an introduction of diffractive MEMS and device theory, followed by the test results of three different designs. The second part of the paper will focus on the polyimide D-MEMS fabrication.

2. Theory of diffractive MEMS

The D-MEMS currently under investigation at the College of Nanoscale Science and Engineering (CNSE) consist of gratings whose rulings can be displaced parallel to the substrate surface. The moving and stationary rulings are called active and passive rulings, respectively. The active rulings are displaced by applying a potential between the rulings and the electrodes underneath. In non-actuation mode, the D-MEMS resemble a normal diffraction grating. The optical effect of displacing a set of rulings is a superposition of the interference patterns of several gratings, depending on the combination of rulings pulled down. This allows for a direct manipulation of the intensity distribution among selected orders.

Figure 1 shows two cross-sections of the D-MEMS. In the non-actuated state, the diffraction pattern corresponds to that of a normal grating. Upon actuation, every other ruling is pulled down a quarter of a selected wavelength. This creates a diffraction pattern in which the original orders are extinguished and additional orders arise, named 'half' orders [6].

As can be seen from the diffraction pattern above, by displacing every other ruling $\lambda/4$, the original orders vanish, while new orders are at their maximum, resulting in optical switching of the signal. The angle of the diffracted orders as well as the displacement required for switching is wavelength sensitive. These properties make the D-MEMS suitable for future optical networks as well as for active spectroscopy.

To achieve commercialization in both the optical interconnect market as well as in planetary spectroscopy, certain parameters have to be optimized: switching at low voltage – devices manufactured at CNSE have achieved switching of $\lambda = 544$ nm light at 10 V with a 13 V bias [7]. This potential should be reduced below 5 V to increase compatibility with IC circuitry. An important parameter for optical interconnects is

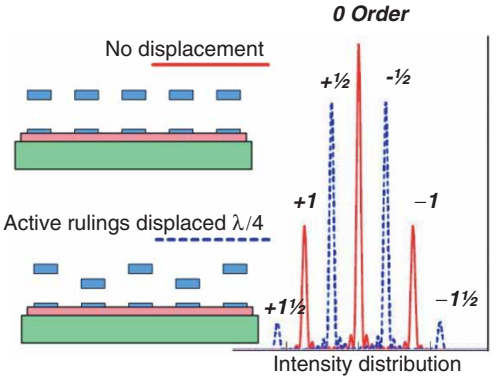

Figure 1. Cross section of D-MEMS in passive state (upper left) and actuated state (lower left), with their corresponding diffraction patterns (right).

switch speed. In order for these devices to enable reconfiguration of the I/O network, it is necessary to switch optically in the microsecond range. In addition, the insertion loss of the device should be reduced to a minimum. The spectral resolution defines the number of channels in an optical fibre. The current goal is to achieve 32 channels in a range of 1220–1620 nm [11].

The optical performance is optimal when active and passive rulings are completely parallel. This uniformity of the grating elements is influenced by residual stress and actuation profile. There are two extremes to model the anchor ruling connection: the 'double-clamped' design is based on either fixed or pinned rulings. A fixed ruling does not allow for any flexibility of the anchor-ruling connection. Pinned rulings allow for rotation of the ruling which better approximates flexible anchors [8].

To investigate ways of reducing the optical switch voltage, a model for electro-mechanical behaviour is derived. The following differential equation is used in which $z(x)$ is the displacement of the ruling along the x-axis, g is the air gap, b is the ruling width, h is the ruling height, E is Young's modulus, V is the voltage, ε_0 is the dielectric constant, and $C_{1,2}$ are constants determined by electrostatic simulations [11], figure 2.

$$\frac{E \cdot b \cdot h}{12} \cdot \frac{d^4 z(x)}{dx^4} = \frac{\varepsilon_0 \cdot b \cdot V^2}{2} \cdot \left(\frac{C_1}{(g + z(x))^2} + \frac{C_2}{b \cdot (g + z(x))} \right) \tag{1}$$

The equation above equates the elasticity of a double-clamped ruling with the electrostatic force between ruling and electrode, allowing for a second term (C_2) which adjusts for non-linear behaviour. The electric field non-uniformity or fringe-field effect arises due to edge effects of the electric field and generally increases the capacitance of the device. To include the fringe-field effect, a simulation of the capacitance is obtained using Intellisuite^{TM}.

The appropriate geometry of the two electrodes is imported from the mask designs, see Table for dimensions. The imported structure is meshed with varying mesh sizes

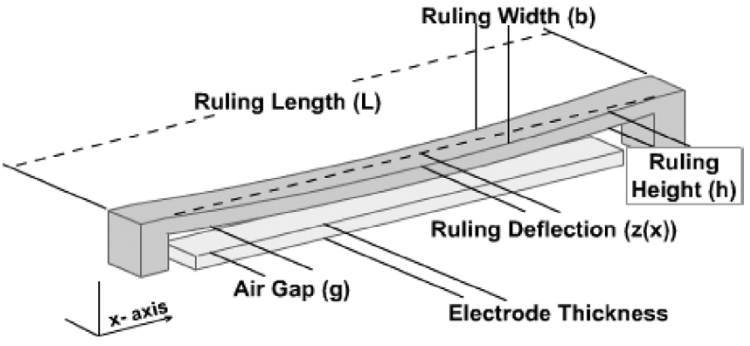

Figure 2. Schematic of ruling.

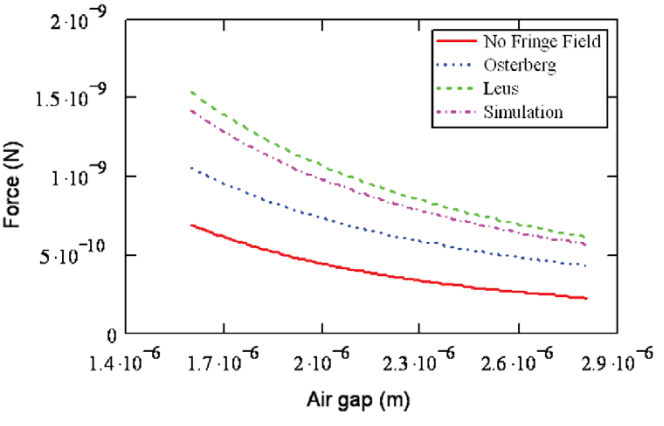

Figure 3. Comparison of analytical equations and simulation of electrostatic force as function of air gap for 2 μm wide ruling-electrode model.

ranging from 0.5 μm in the centre to 0.125 μm at the edges where a larger change in charge distribution is expected. The capacitance at five different air gap values (2.75–1.65 μm) is simulated. A linear regression was applied to the reciprocal of these capacitance simulation points, which generated a capacitance function with good fit (corr. > 0.99).

The electrostatic force, including the fringe field effect, is then derived from this capacitance function. The constants C_1 and C_2 are found to be 1.427 and 0.781, respectively. The simulation results are plotted in figure 3 and are compared to analytical equations obtained from Osterberg *et al.* [9] and Leus *et al.* [10]. Osterberg *et al.* have derived their formula also based on computer simulations, but do not mention electrode height. Leus *et al.* have derived their equation purely analytically and have included electrode height. The simulation was repeated for a width of 3 and 4 μm. The corresponding constants can be found in table 2. By utilizing the spring constant, a function can be derived that predicts operation voltage as function of centre ruling displacement. This function is highly dependent

Table 1. Dimensions of rulings used in capacitance simulations.

Dimensions used in simulation	
Ruling/electrode length	200 μm
Ruling/electrode width	2,3, and 4 μm
Ruling thickness	1.5 μm
Electrode thickness	0.5 μm
Air gap	Five incremental steps from 1.65 to 2.75 μm

Table 2. Constants for electrostatic force including fringe-field effect.

	C_1	C_2
No fringe field	1	0
Simulation, 2 μm width	1.427	0.781
Simulation, 2 μm width	1.294	0.823
Simulation, 2 μm width	1.224	0.858
Osterberg, 2 μm width	1	0.65

on the applied boundary conditions: a double-pinned ruling is five times more flexible than a double-fixed ruling [8].

For steady state deflection of the ruling as a function of applied voltage, a low spring constant is required. For fast switching speeds, a high spring constant, increased thickness (h) with small ruling length (L) is required. See equation (2) for the natural frequency of a doubly clamped ruling in which ρ is the mass density of the ruling material. These requirements are contrary to those for steady state deflection. In order to increase switch speed while decreasing steady state operation voltage, the electrostatic force is increased by increasing the capacitor area.

$$f = \frac{\pi}{2L^2} \times \sqrt{\frac{E \cdot h^2}{12 \cdot \rho}} \tag{2}$$

Equations (3)–(5) contain the optical theory derivation of the aforementioned optical switching. The variables of the equations are as follows: θ is the diffraction angle, ϕ is the incident angle, b is the width of each ruling, d is the periodicity of the grating, N is number of rulings, and Δ is the displacement of the active rulings. δ describes the diffraction pattern of a single ruling. χ_p and χ_a describe the interference pattern of the passive and active rulings, respectively. Equation (6) presents the intensity distribution of the D-MEMS device; the first three terms describe the distribution of a normal grating with double the periodicity, the last term, which includes χ_a, extinguishes the half orders when $\Delta = 0 \bmod \lambda/2$, or extinguishes the whole orders when $\Delta = \lambda/4 \bmod \lambda/2$ [1, 11].

$$\delta_{(\theta,\varphi)} = \frac{\pi \cdot b}{\lambda} \cdot [-\sin(\theta) - \sin(\varphi)] \tag{3}$$

$$\chi_{p(\theta,\varphi)} = \frac{\pi \cdot d}{\lambda}[-\sin(\theta) - \sin(\varphi)] \tag{4}$$

$$\chi_{a(\theta,\varphi)} = \frac{\pi}{\lambda}[d \cdot (-\sin(\theta) - \sin(\varphi)) + \Delta \cdot (\cos(\theta) + \cos(\varphi))] \tag{5}$$

$$I_{D-MEMS(\theta,\varphi)} = I_0 \cdot \left(\frac{\sin(\delta_{(\theta,\varphi)})}{\delta_{(\theta,\varphi)}}\right)^2 \cdot \left[\frac{\sin(N\chi_{p(\theta,\varphi)})}{\sin(2\chi_{p(\theta,\varphi)})}\right]^2 \cdot (2cos(\chi_{a(\theta,\varphi)}))^2 \tag{6}$$

Spectral resolution is a critical parameter in optical interconnects and spectroscopy. Resolution based on the Rayleigh criterion (R_λ) depends on the number of rulings N and diffraction order m ($m = 0, \pm ½, \pm 1, \pm 1½, \ldots$), see equation (7). Because the spectral resolution is directly proportional to the number of periods of the D-MEMS, extra care needs to be taken to allow for optically flat diffractive surfaces. Because the grating is suspended, residual stresses in the structural layer will result in buckling which decreases the useful optical area of the device.

A future goal is to create high spectral resolution D-MEMS devices with 32 channels in the range of 1220–1620 nm [11]. Based on equation (7) and $m = ½$ diffraction order, a minimum of 227 rulings need to be illuminated. Current prototypes incorporate 40 rulings, a higher resolution while maintaining an optically flat surface will be achieved by integration of seamless diffractive optical elements into a large array.

$$R_\lambda = \frac{\lambda}{m \cdot N} \tag{7}$$

Another optical parameter of interest is insertion loss. This can be divided in three parts: material reflectance, fill factor, and diffracted order power. The first term can be increased by adding a gold layer on top of the polysilicon ruling making it more reflective. The second term is defined by the geometry of the device. The fill factor is ½ when the grating period is twice the ruling width. The third term is obtained by integrating the diffraction pattern, as given in equation (6), between both minima at each side of the diffracted order. Given a wavelength of 1550 nm, the normalized diffracted power for orders 0 and 1 are 44.6% and 19.6%. At an active ruling displacement of $\lambda/4$, the normalized diffracted power for orders ½ and 1½ are 36.8% and 4.8% respectively [11].

3. Polysilicon surface micromachining

Silicon based D-MEMS devices are fabricated at MEMSCAP using the Multi-User MEMS Process (MUMPS). This is a three polysilicon layer surface micromachining process. Process conditions have been optimized and material properties are provided by the fabrication company. This allows for quick and robust testing of new design ideas. The process starts with a blank Si wafer with nitride deposited for electrical isolation, followed by three polysilicon structural layers (poly0, poly1 and poly2) and

two phosphosilicate glass (first oxide and second oxide) sacrificial layers in between; this is followed by the deposition of a metal layer [11].

3.1. *Design overview*

The initial, 'double-clamped' design consists of a suspended grating above active and passive electrodes. The active electrodes can be biased with respect to the grating, resulting in downward deflection of every other ruling. This design is limited in that the profile is altered upon actuation, reducing the effective optical area. In order to increase the steady state actuation deflection, the ruling length needs to be increased. This increases the residual stress buckling which affects the flatness of the surface. The width of the ruling is 2 μm, 1.5 μm height, and 220 μm long. The air gap between top and bottom electrode is 2.75 μm as shown in figure 4(a) [7].

The second, 'cantilever-suspension', design introduces two flexible cantilevers at each end of a connected set of rulings. The ruling width is increased to 4 μm to make room for passive rulings in between. The cantilevers are 2 μm wide and 50 μm long. The ruling length is 230 μm. The connection between the rulings also increases the capacitive area. Three dimples are placed on the ruling to reduce the possibility of stiction. At the centre of the ruling, this decreases the air gap from 2.75 to 2.10 μm. Passive rulings are placed between the openings of the active frame. For certain designs, a gold layer is applied on top of the rulings to increase reflectivity, figure 4(b).

The third, 'double grating', design consists of a suspended grating with double periodicity above a lower grating with normal periodicity, which also acts as the lower

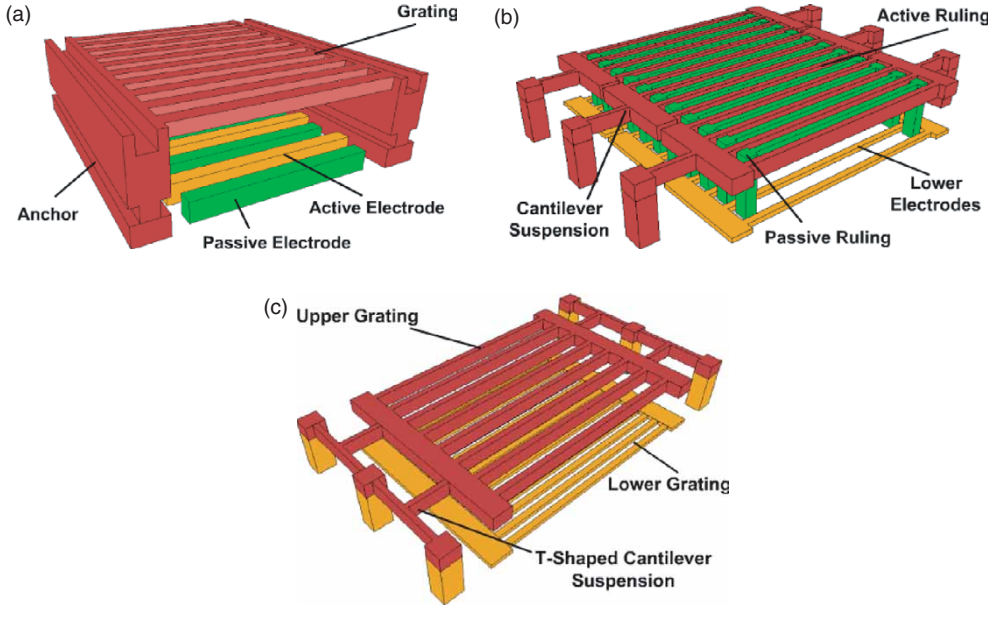

Figure 4. Schematic (not to scale) of: (a) Double-Clamped design, (b) Cantilever-Suspension design, and (c) Double Grating design.

electrode. The lower grating acts as reflective rulings as well as electrostatic actuators. The ruling width of these devices is 2 μm. Ruling lengths vary from 150 to 230 μm, figure 4(c) [7].

4. Testing and characterization

Figure 5(a) shows a scanning electron microscope (SEM) image of a 'double-clamped' design. The White Light Interferometer (WLI) results of these devices, which were taken at ZYGO, Middlefield CT, show the flatness of the diffraction rulings. In figure 5(b), a cross-section derived from optical surface profile measurements is shown with, on average, a 60 nm centre ruling buckling. The dimple pattern is introduced in all polysilicon designs to minimize stiction. The optical test results are shown in figure 6. Because of differences in residual stress buckling of active and passive rulings, the initial condition shows a state in between optical switching. Optical switching is achieved at 11 V ramp at 13 V bias [13].

The 'cantilever-suspension' devices with a gold layer on the rulings showed high buckling which was verified using the WLI. This measurement revealed a static, downward displacement of ~1.3 μm at the centre of the ruling (see figure 7) [13]. Optical

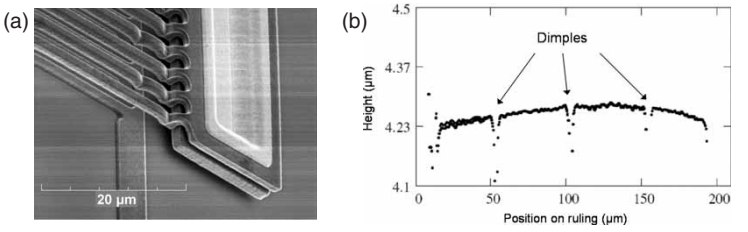

Figure 5. Double-Clamped device results: (a) SEM image showing the anchor and rulings, (b) WLI result showing 80 nm centre ruling buckling on average.

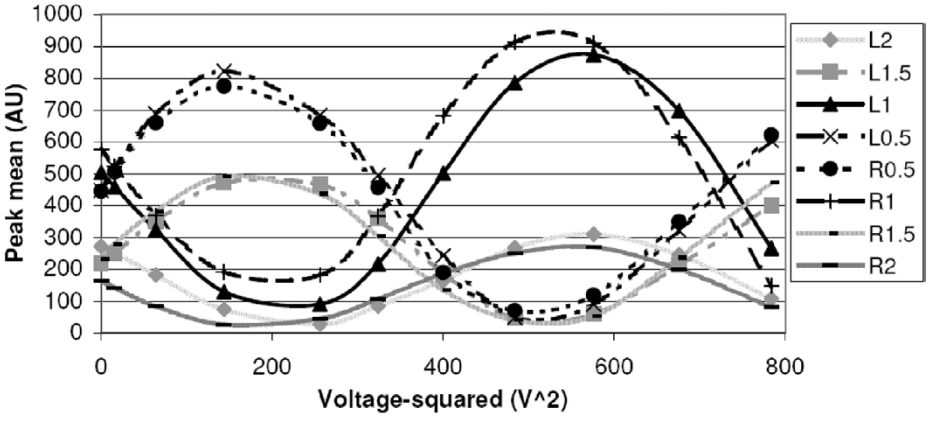

Figure 6. Switching behaviour of Double-Clamped device.

experiments showed no movement at the centre of the rulings, but movement was observed at the ruling ends. Unbalanced residual stress of the gold and polysilicon layer led to erratic operation of these initial prototypes. For 'cantilever-suspension' devices without gold the residual stress resulted in upward buckling. These devices did show good actuation results. Optical switching results verified a significant reduction in the operation voltage to 6 V ramp at 8 V bias as shown in figure 8.

The 'double grating' design (figure 4c) is fabricated and is currently undergoing testing. Preliminary laser vibrometer measurements show good electro-mechanical behaviour. The centre of the rulings show displacement of ~800 nm compared to the 150 nm of 'cantilever-suspension' based devices discussed above (see figure 9). Initial optical results show a large reduction in the actuation voltage (i.e. 2 V ramp at 6.5 V bias) as shown in figure 10.

The 'double-clamped' polysilicon D-MEMS shows a low amount of buckling due to residual stress. It achieves switching at a 10 V ramp with a 13 V bias. The 'cantilever-suspension' devices reduce the optical switching potential to a 6 V at an 8 V bias. The 'double grating' design shows a high ruling displacement of 800 nm at 12 V

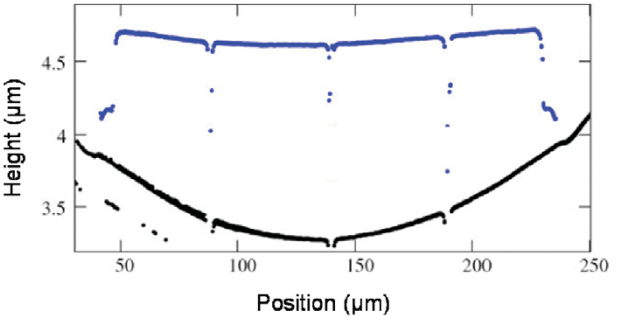

Figure 7. WLI result of cantilever-suspension design showing difference in buckling due to residual stress of passive (upper) and active (lower) rulings.

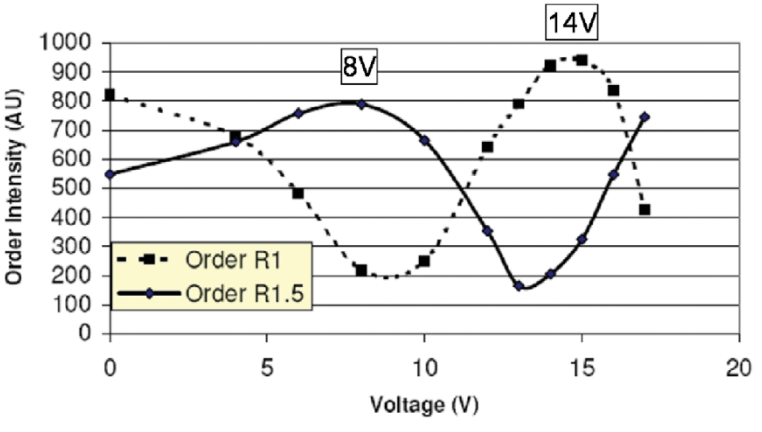

Figure 8. Optical switching results of Cantilever-suspension design.

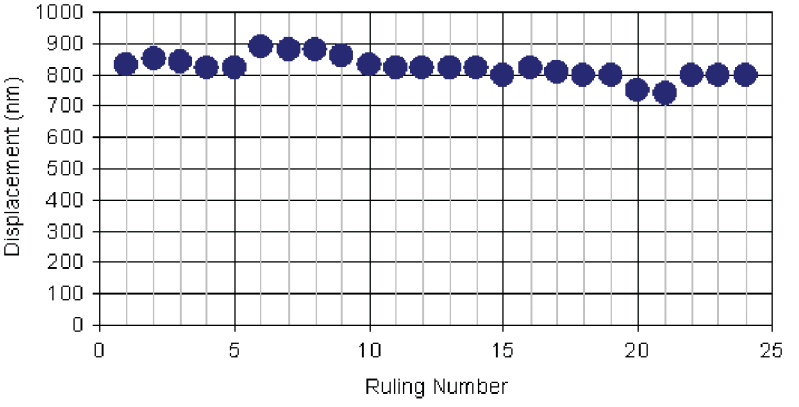

Figure 9. Laser vibrometer results of double-grating design, at 12V applied potential.

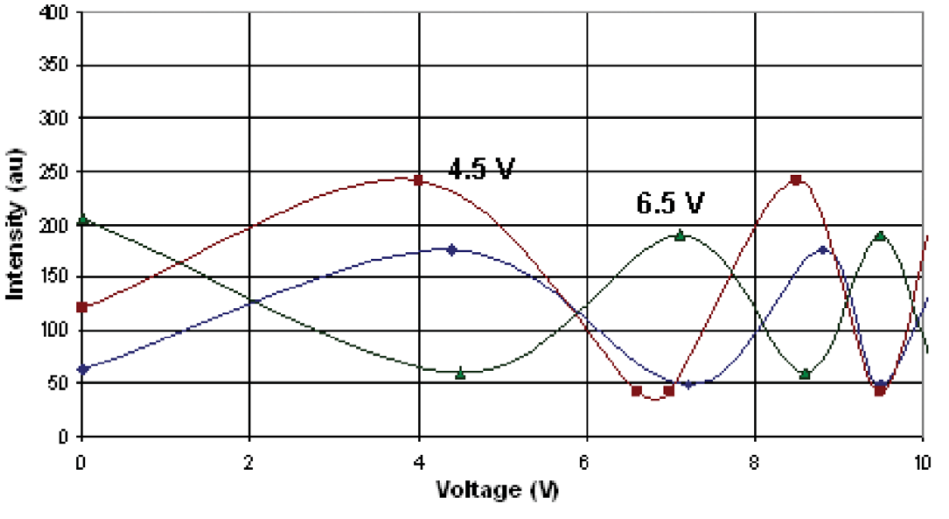

Figure 10. Optical test results of double grating design.

applied potential. Preliminary optical measurements show optical switching of 2 V with 6.5 V bias.

5. Polyimide MEMS fabrication and optimization

The Young's modulus of polysilicon used for diffractive MEMS is very high: ~158 GPa [12]. A design modification was investigated to lower the switching voltage by utilizing polyimide as the structural material. The process would allow for in-house fabrication for a higher control of layer thickness and other process parameters. The first generation of devices, reported by Castracane *et al.* [6], show initial actuation voltage reduction of 8 V compared to their polysilicon counterparts which were switching at

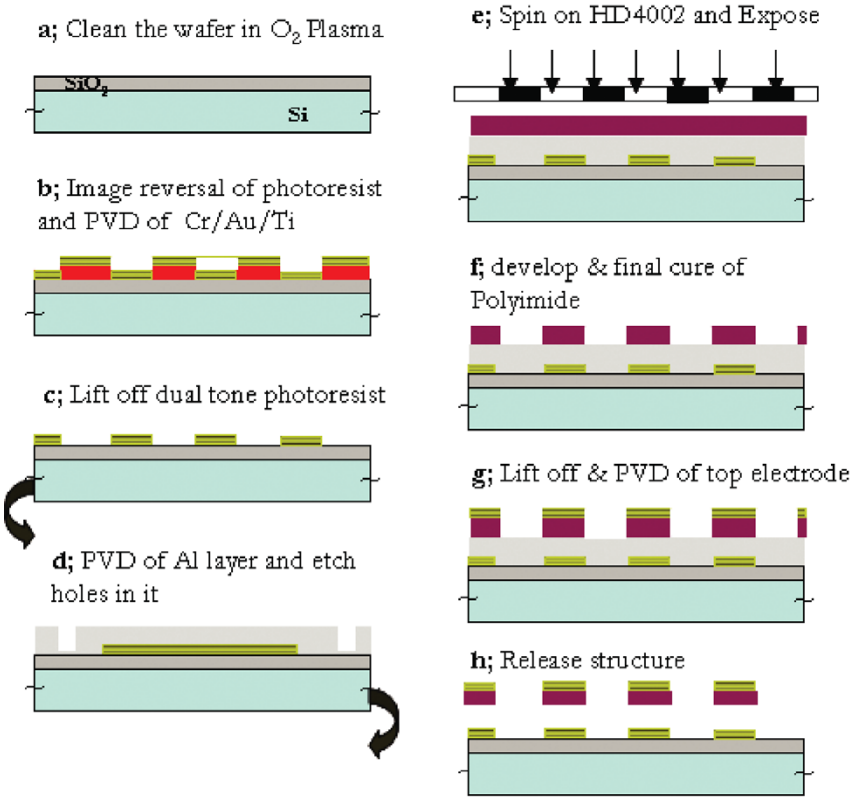

Figure 11. Polyimide D-MEMS process flow.

24 V. The current polyimide device being optimized is based on the polysilicon 'double-clamped' design.

The polyimide used in the process is HD 4002 manufactured by HD Microsystems™. HD 4002 is a negative-tone, solvent developed, and I-line photo definable polyimide. The final cured polyimide film has a 3.5 Gpa Young's modulus, 35 Mpa residual stress, and a glass transition temperature of 350°C [12].

The full process flow for the polyimide devices is shown in figure 11 and will be discussed in detail in the following.

The dimensions of the polyimide grating are: length 130 μm and 200 μm, width 4 μm and a period of 8 μm. The thickness of the device's structural and sacrificial layers can be controlled by adjusting process parameters. The wafer fabrication process is based on four chromium masks.

SiO_2 is thermally grown on the wafer to electrically isolate critical parts of the device and to act as an optical absorption layer. The fabrication starts by defining the bottom electrode consisting of three metal layers: chromium (Cr), gold (Au) and titanium (Ti) of thicknesses 20 nm, 100 nm, and 30 nm, respectively. Au is the bottom electrode (utilized for its high conductivity), Cr is used to promote the adhesion and Ti is used as protection layer. Dual tone photoresist AZ 5206 (Shipley™) is spun on the wafer

followed by a soft bake and photolithographically exposed. The wafer is heated to 115°C for 3 minutes for a hard bake followed by flood exposure to reverse the image after which it is developed. Physical Vapour Deposition (PVD) of the Cr, Au and Ti takes place using electron beam (e-beam) evaporation tool. Lift-off is performed by etching the photoresist in ultrasonic agitation, figure 11.

The second step is to define the gap between the bottom electrode and the polyimide rulings. This is done by depositing aluminium (Al) using the same e-beam tool. Al will act as a sacrificial layer for the polyimide grating. Post-holes are etched into the aluminium which will anchor the polyimide to the substrate. This is done by patterning a positive tone photoresist (Shipley^{TM} 1813) with the next mask. After exposure and developing of the 1813, Al is wet etched with phosphoric acid, nitric acid, acetic acid and de-ionized water in the ratio developing of 15:1:1:1 (see figure 11d and figure 12).

The third step is to pattern the polyimide ruling. HD 4002 is spin coated on the sacrificial layer. Two-step spin speed process is used to achieve final film thickness of 2 μm: 300 rpm/7 sec + 2800 rpm/30 sec [14]. Polyimide is very sensitive to humidity during the spinning operation. Humidity reacts with the polyimide causing it to precipitate out in extreme cases. Spin coating of polyimide is followed by pre-baking and exposed with the third mask. The polyimide should be held for 45 minutes at room temperature to stabilize and harden the exposed region prior to development for optimal side-wall angle. The exposed polyimide film is developed using PA400D developer solution and immediately followed by immersion in a 1:1 mixture of developer and rinser (PA400R). The final rinse is performed by immersion in PA400R solution.

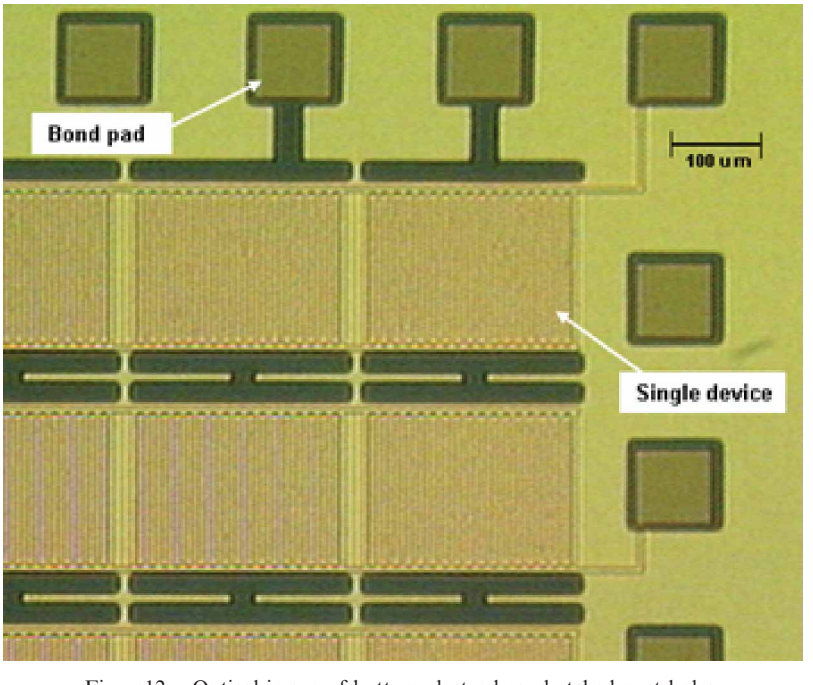

Figure12. Optical image of bottom electrode and etched post holes.

The polyimide device layer then needs to be cured. In this process step, the residual solvents are removed, the imidization process is completed, the photopolymer cross links are removed and SiO_2 adhesion is completed. This curing cycle is done in a nitrogen rich environment at low pressure and 350°C (see figure 11e, f and figure 13). The scumming of polyimide in the field due to the reflow during final cure (see figure 13b) is a typical problem in polyimide processing. This is solved in the last step in which the wafer is placed in an oxygen plasma tool to etch the reflowed polyimide in between the ruling region. HD 4002 is a dielectric polyimide, so a thin layer of metal is deposited on top which will act as the top electrode and increase the reflectance of the device.

The fourth step is similar to the first step. AZ5214 (Shipley^{TM}) dual tone photoresist is used for image reversal. A thick layer is required for a high aspect ratio. The top metal consists of Cr (20 nm) and Au (120 nm). Au is the top electrode and reflective layer. AZ5214 is exposed with mask 4 after a soft bake. The alignment in this step is very critical. After image reversal, Cr and Au are deposited using e-beam followed by lift-off (figure 11f). The aluminium layer is released by wet etching using phosphoric acid, nitric acid and acetic acid as described earlier. This is followed by cleaning with de-ionized water, iso-propanol and hexane. Hexane has a low surface tension which reduces the chance of stiction, figure 11(h) and figure 14.

The polyimide D-MEMS are in the final phases of fabrication and packaging of new devices is underway. Optical and mechanical characterization will verify the possible decrease in the voltage required for optical switching by using a more flexible structural material. The polyimide process flow will be further optimized for other areas of design improvement such as switch speed and spectral resolution.

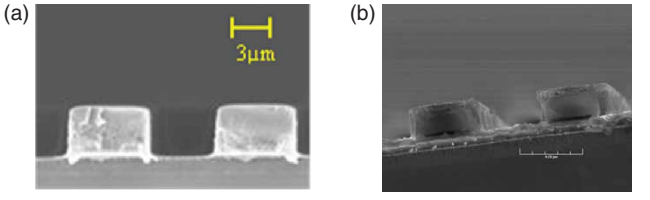

Figure 13. Cross-sectional SEM of polyimide rulings before (a) and after cure (b).

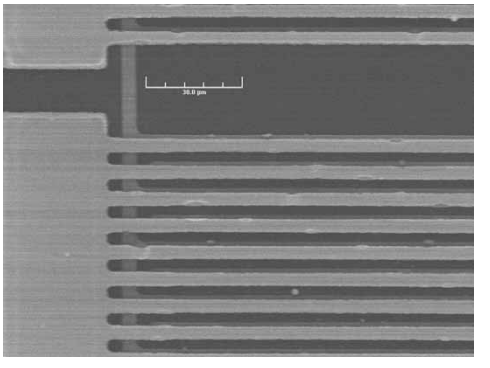

Figure 14. Top down SEM of the edge of single device after release.

6. Conclusion

Important aspects of silicon based diffractive MEMS (D-MEMS) devices are listed and investigated. Optical test results from the last three designs show an improvement in switching voltage from 11 V ramp at a 13 V bias to a 2 V ramp at 6.5 V bias for 544 nm for the 'double grating'-based designs. The electromechanical testing of the 'double grating' designs show vertical displacement of 800 nm at 12 V. The fabrication process of polyimide diffractive MEMS is explained step-by-step with process results. Polyimide based MEMS devices have been manufactured, diced and released, and will undergo future experimental testing.

Acknowledgments

The authors would like to thank Larry Clow Jr and Natalaya Tokranova from CNSE for their help on polyimide processing and Stephen Kobak from ZYGO™ for his help in obtaining white light interferometer data.

References

[1] J. Castracane, M. Gutin. MEMS-based micrograting: preliminary results of novel configurations. *Proceedings. Miniaturized System with Micro-Optics and Micromechanics III*. San Jose, CA. Vol. 3276, pp. 196–206, January (1998).
[2] Y. Ito, K. Saruta, H. Kasai, M. Nishida, M. Yamaguchi, K. Yamashita, A. Tag. High-performance blazed GxL device for large-area laser projector. *Proc. MOEMS Display, Imaging, and Miniaturized Microsystems*. Ed:. Vol. 6114, pp. 1–12. SPIE (2006).
[3] Polychromix Technical Paper. MEMS Based Digital Transform Spectrometer. http://polychromix.com 30 Upton Drive, Wilmington, MA 01887, USA (February 2, 2006).
[4] J. Trisnadi, C. Carlisle and R. Monteverde. Overview and applications of Grating Light Valve based optical write engines for high-speed digital imaging. *Proc. MOEMS Display and Imaging Systems*. Ed:. Vol. 5348, pp. 52–64. SPIE (2004).
[5] Guoqiaug li, Dawei Huang, Emal Yuceturk, Philippe J. Marchand, Sandik C. Esener, Volkan H. Ozguz and Yue Liu. Three-dimensional optoelectronics stacked processor by use of free-space optical interconnection and three-dimensional VSLI chip stacks. *Appl. Opt*., **41**, 348 (2002).
[6] J. Castracane, D. Yang, S. Madison, G. Panaman, B. Xu. Low power MOEMS components for active optical system. *J. Microlithog, Microfab. Microsyst*., **4**, 4 (2005).
[7] J. Verheggen, G. Panaman, W. Khan Raja, J. Castracane. Optimization of diffractive MEMS for optical switching. *Proceedings. MEMS, NEMS & Sensing*, Boston, MA. Vol. 3, pp. 401–404. NSTI (2006).
[8] J.A. Pelesko, D.H. Bernstein. *Modeling MEMS and NEMS*. Chapman & Hall/CRC, Boca Raton, FL (2002).
[9] Peter M. Osterberg, Stephen D. Senturia. M-TEST: A test chip for MEMS material property measurement using electrostatically actuated test structures. *J. Microelectromechan. Syst*., **6**, 107 (1997).
[10] Fringing Field Effect in Electrostatic Actuators. TECHNION. May, 2004. < http://oldmeeng.technion.ac.il/Research/TReports/index.html >
[11] Jaap P. Verheggen. Optimization of the micro-electro-mechanical systems (MEMS) compound grating. MS thesis, State University of New York-Albany (2006).
[12] D. Koester, A. Cowen, R. Mahadevan, M. Stonefield, B. Hardy. *PolyMUMPs Design Handbook Rev*. 10.0. MEMSCAP (2003).
[13] J. Verheggen, G. Panaman, J. Castracane. Characterization and Fabrication of MOEMS-based Diffractive Optical Switching Elements. *Proceedings. MOEMS Display, Imaging, and Miniaturized Microsystems IV*. San Jose, CA. Vol. 6114, pp. 139–47 (2006).
[14] Product bulletin. Photo definable HD 4000 series Polyimide. HD MicroSystems, 500 Cheesequake Rd. Parlin, NJ 08859, USA. http://hdmicrosystems.com